Inclusive soft pion production from 12.3 and 17.5 GeV/c protons on Be, Cu, and Au

I. Chemakin,[2] V. Cianciolo,[7,8] B. A. Cole,[2] R. A. Fernow,[1] A. D. Frawley,[3] M. Gilkes,[9] S. Gushue,[1] E. P. Hartouni,[7] H. Hiejima,[2] M. Justice,[5] J. H. Kang,[11] H. G. Kirk,[1] N. Maeda,[3] R. L. McGrath,[9] S. Mioduszewski,[10,1] D. Morrison,[10,1] M. Moulson,[2] M. N. Namboodiri,[7] R. B. Palmer,[1] G. Rai,[6] K. Read,[10] L. Remsberg,[1] M. Rosati,[1,4] Y. Shin,[11] R. A. Soltz,[7] S. Sorensen,[10] J. H. Thomas,[7,6,1] Y. Torun,[9,1,12] D. L. Winter,[2] X. Yang,[2] W. A. Zajc,[2] and Y. Zhang[2]

[1]*Brookhaven National Laboratory, Upton, New York 11973*
[2]*Columbia University, New York, New York 10027*
[3]*Florida State University, Tallahassee, Florida 32306*
[4]*Iowa State University, Ames, Iowa 50010*
[5]*Kent State University, Kent, Ohio 44242*
[6]*Lawrence Berkeley National Laboratory, Berkeley, California 94720*
[7]*Lawrence Livermore National Laboratory, Livermore, California 94550*
[8]*Oak Ridge National Laboratory, Oak Ridge, Tennessee 37831*
[9]*State University of New York at Stony Brook, Stony Brook, New York 11794*
[10]*University of Tennessee, Knoxville, Tennessee 37996*
[11]*Yonsei University, Seoul 120-749, Korea*
[12]*Illinois Institute of Technology, Chicago, Illinois 60616*

(Received 5 August 2001; published 14 January 2002)

Differential cross sections are presented for the inclusive production of charged pions in the momentum range 0.1–1.2 GeV/c in interactions of 12.3 and 17.5 GeV/c protons with Be, Cu, and Au targets. The measurements were made by Experiment 910 at the Alternating Gradient Synchrotron (AGS) at Brookhaven National Laboratory. The cross sections are presented as a function of pion total momentum and production polar angle θ with respect to the beam.

DOI: 10.1103/PhysRevC.65.024904 PACS number(s): 13.85.Ni, 25.40.Ve

I. INTRODUCTION

Pions are copiously produced in hadronic interactions at high energies. However, because of the complexity of soft hadronic interactions, theoretical descriptions of pion spectra in elementary hadronic interactions are difficult to obtain. The situation with pion production in proton-nucleus collisions is even more difficult because of the contributions from the multiple interaction of the projectile proton and potential final-state interactions of the outgoing pions with the nuclear target. At low momentum these final-state interactions are expected to be dominated by the low-lying baryon resonances that are thought to also play an important role in nucleus-nucleus collisions at Alternating Gradient Synchrotron (AGS) and lower energies. Precise measurements of pion spectra at low momentum may then provide new insight into the role of these resonances and may help constrain event generators [1,2] that have been used to set a baseline for new phenomena in heavy-ion collisions.

Detailed knowledge of pion spectra at low momentum is also of great practical importance since the production of intense muon beams at potential new high-energy facilities such as muon colliders [3] and neutrino factories [4,5] relies on the decay of pions produced in a nuclear target. The strong increase in pion yields at very low momentum resulting from the excitation and decay of baryonic resonances in the target may provide the necessary yield per beam proton to make such facilities attractive. Experimental measurement of these spectra is crucial to evaluating the feasibility of generating such intense beams.

Unfortunately, existing data in the low-momentum region (<200 MeV/c) are limited due to lack of statistics, acceptance, or the particle identification capabilities of previous experiments [6–10]. Experiment 910 (E910) is the first experiment at the AGS to provide a large-statistics data set that covers a large angular range at low momentum and to provide particle identification over its entire acceptance. It thus provides an unprecedented opportunity to fill the gap in our knowledge of pion production in proton-nucleus interactions.

II. EXPERIMENT

Experiment 910 ran for 14 weeks at the MPS facility in the $A1$ secondary beamline of the BNL AGS in 1996. Figure 1 shows part of the detector layout pertinent to the inclusive pion production measurement. The total momenta and directions of incoming beam particles were reconstructed using proportional chambers located in the beamline upstream of the target. Three threshold Cerenkov counters along the beamline were used to reject particles in the beam other than protons. A set of trigger counters ($S1$,ST) and veto counters ($V1$,$V2$) located between the proportional chambers and the target were used to detect and constrain the trajectories of incoming beam particles. These are shown in Fig. 2. The Au, Cu, and Be targets were rectangular with 5×5, 6.35×6.35, and 7.62×2.54 cm^2 cross section and 3.9, 4.1, and 3.4 g/cm^2 thickness, respectively. The beam spot on the target was defined by the last veto scintillator that had a 2×1 cm^2 slot with semicircular ends.

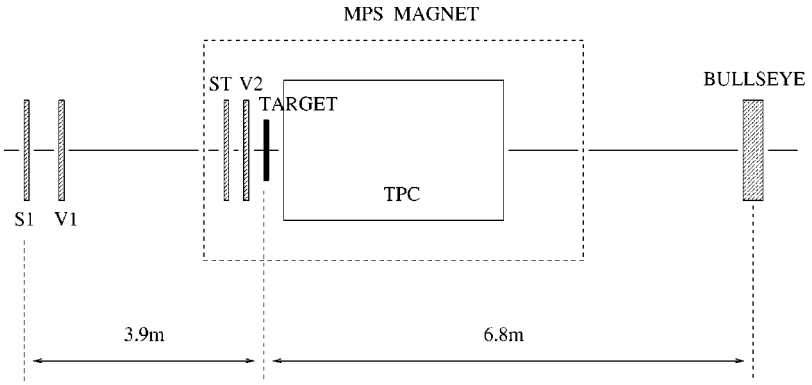

FIG. 1. E910 detector layout for this measurement (not to scale). Beam comes in from the left toward the target located in front of the TPC.

The EOS time projection chamber (TPC) [11] was placed inside the MPS magnet with its active gas volume about 10 cm downstream of the target and with its long axis (z) approximately aligned with the incoming beam direction. It contains 15 360 pads of size 0.8×1.2 cm^2 arranged in 128 transverse (x) rows with 120 pads each to give a 96×153.6 cm^2 footprint for the pad plane. The total vertical drift distance used for recorded ADC samples was 70 cm. The magnetic field had a strength of 0.5 T and was oriented along the vertical (y) direction. A vertical electric field of 120 V/cm supplied the drift force on electrons from ionization by charged tracks in the $P10$ gas at atmospheric pressure. Pad signals were sampled by 12-bit ADCs every 100 ns. Signals from charged tracks were reconstructed as hits in the TPC centered on padrows in z with the x position given by a charge weighted mean of the signal from several pads in a row and the y position calculated by the offset from a Γ function fit to the time dependence. Reconstructed hit positions were corrected for shifts due to inhomogeneities in the magnetic field before tracking. Simultaneous track finding and momentum reconstruction with a fixed radius helical fit [12] was followed by primary vertex reconstruction [13] by projecting the beam track forward and TPC tracks back to the target. Track momenta were then refit using the magnetic field map. The trigger of the production results in this paper was obtained by requiring the absence of a beam particle in a downstream ''bullseye'' counter. This counter consisted of two pairs of scintillator slats, one pair of 14.6×30.5 cm slats placed along the vertical and the other 40.6×7.6 cm pair along the horizontal. Beam particles consistent with the aperture defined by the veto counters were entirely located within the intersection of one of the horizontal and one of the vertical slats as shown in Fig. 2. In addition to about 4 000 000 minimum bias bullseye triggers, a set of pure beam triggers was also recorded and used to study potential biases in the bullseye trigger and to check the normalization of the spectra. A large fraction of bullseye triggers came from interactions well downstream of the target due to material in the beam path (including wire chambers and a Čerenkov detector located between the TPC and bullseye, as well as the TPC gas).

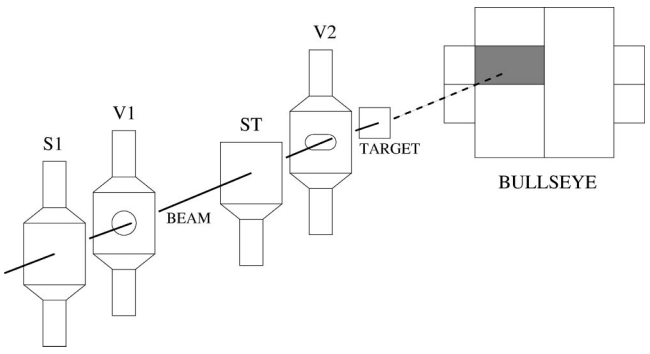

FIG. 2. Beam trigger for minimum bias production measurement is defined as $S1\cdot\overline{V1}\cdot ST\cdot\overline{V2}$. Shaded area on the bullseye defines the beam veto region.

III. DATA ANALYSIS

We required a minimum of ten hits in the TPC for charged tracks associated with the vertex. We also required the reconstructed primary vertex to be consistent with the target position and the $V2$ veto hole. Interactions were identified as events with a successfully reconstructed vertex with at least two charged tracks in the TPC. Two-prong events consistent with a beam track and a δ electron from the target were removed from the interaction sample. After these cuts, there were 16.5–79 K events in the bullseye trigger samples for the six data sets. Table I shows the event statistics. The primary method of particle identification used for slow pions was ionization energy loss dE/dx. Figure 3 shows dE/dx as a function of momentum below 1.4 GeV/c. Note the over-

TABLE I. Event statistics and overall normalization factor for different data sets.

Beam momentum	Target	Number of interactions	Correction factor
17.5 GeV/c	Au	32121	1.052
	Cu	54591	1.033
	Be	78927	1.080
12.3 GeV/c	Au	16522	1.023
	Cu	36891	1.096
	Be	41790	1.040

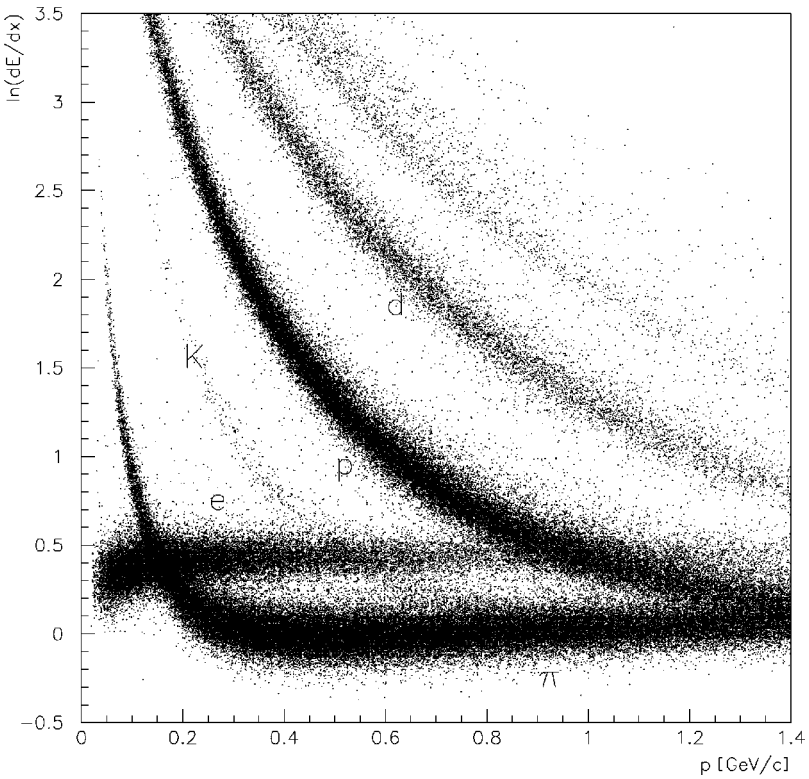

FIG. 3. dE/dx as a function of momentum showing particles that can be identified in different bands.

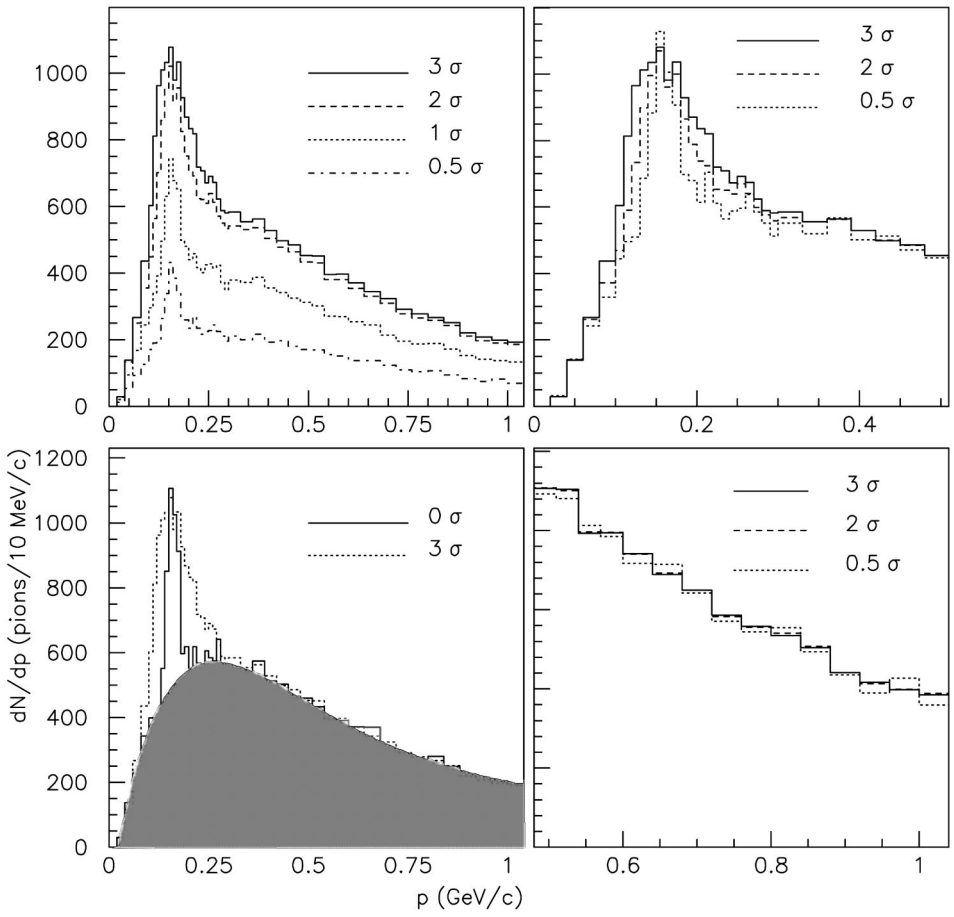

FIG. 4. Electron background subtraction illustrated in one dimension. Top left panel shows momentum distributions in the pion band for different widths in dE/dx. The top and bottom right panels show the low and high momentum half of the histograms obtained by scaling these according to the area of a Gaussian within a given width. Note the shrinking overlap and matching tails. Extrapolation to zero width gives the narrowest histogram shown in the bottom left panel together with the original 3σ distribution (dotted line) and the fit (solid line) used to remove the background spike on top of the smooth pion spectrum (shaded area).

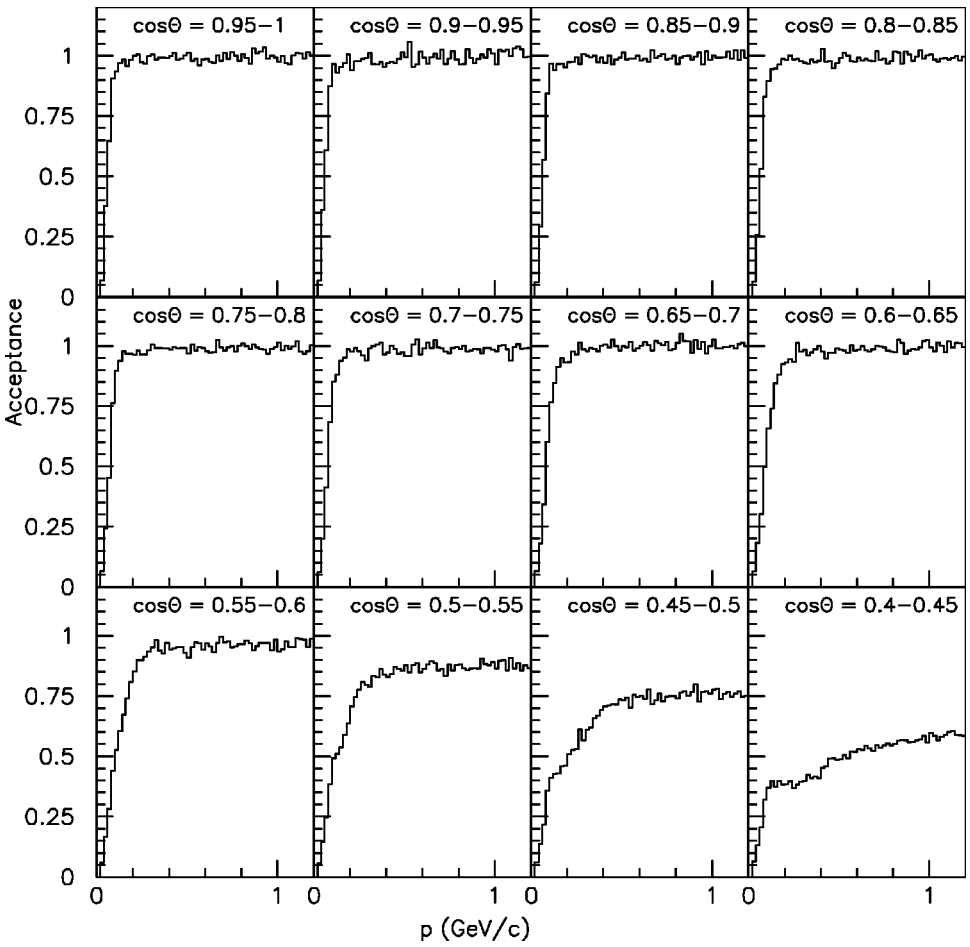

FIG. 5. TPC acceptance for positive pions coming out of the Au target from GEANT simulation as a function of momentum from 20 to 1200 MeV/c in 0.05-wide cos θ bins.

lap of the pion band with the proton band above 1.2 GeV/c and the overlap of pions in the 100–200 MeV/c range with electrons/positrons resulting primarily from pair production through photon conversions in the nuclear targets. The dE/dx for each track was calculated using a 5–65 % truncated mean after discarding any hits that were shared with other tracks. A residual shift of the truncated mean with the number of samples was corrected for using a quadratic fit and the resulting distributions were very nearly Gaussian.

To resolve the particle identification ambiguity in the low-momentum overlap region, we used the following simple method illustrated in Fig. 4. First we took momentum distributions with progressively narrower cuts on the dE/dx width around the pion band, 3σ, 2σ, 1σ, etc. These have the electron background confined to a shrinking region of momentum. Then we extrapolated the resulting distributions to zero width after proper scaling. Finally we fit the extrapolated distribution and subtracted the electron component. In this fit, we used the product of an exponential and a third order polynomial for the pion distribution and a Gaussian for the electron distribution. The width extrapolation and acceptance correction were done in two dimensions ($p-\cos\theta$), whereas the two-component fitting was carried out on one dimensional momentum projections.

The geometric acceptance of the TPC covers most of the forward hemisphere. We applied fiducial cuts to the data to exclude regions where the acceptance is less than 10%. The full acceptance, shown in Fig. 5 was calculated by running 8 000 000 pion tracks for each target through a GEANT simulation of our experiment, which included all the relevant processes (energy loss, multiple scattering, decay) as well as hit and track reconstruction efficiencies. We also ran 1 000 000 17.5 GeV/c p-Au events generated by RQMD [2] through the simulation to evaluate multitrack effects.

A lower momentum cutoff of 100 MeV/c was set by requiring the momentum resolution from multiple scattering and energy loss to be below 5%. This is well within the geometric acceptance. The 1.2 GeV/c limit at the other end is due to the dE/dx overlap between protons and pions. We picked bin sizes in momentum (100 MeV/c) and cos θ (0.1) to keep the statistical uncertainty in each bin below 20%. The 100–200 MeV/c bin is further split in two (100–140 and 140–200 MeV/c), in cases where the electron pion overlap was restricted to the 140–200 MeV/c region. Our momentum resolution ranges from 2% at 1.2 GeV/c to 4.5% at 100 MeV/c. The decay loss in the lowest-momentum bin is less than 4%. Multitrack effects contribute less than 5% to the uncertainty in production results. Also, we estimate the effect of reinteraction and pion absorption in the target to be less than 5% each based on simulations.

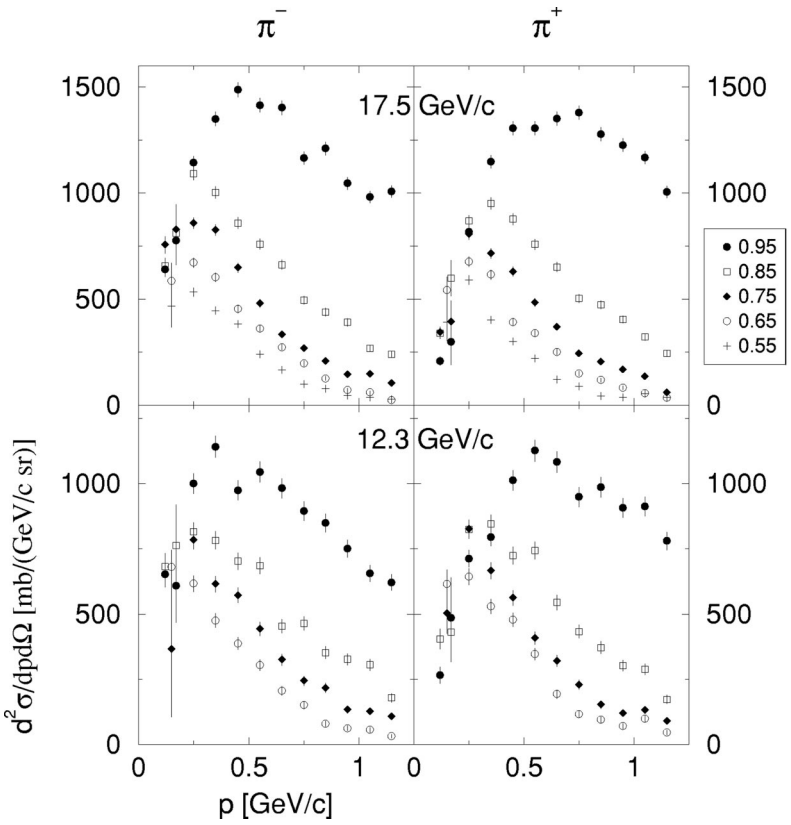

FIG. 6. Production cross sections for π^- (left column) and π^+ (right column) from p-Au at 17.5 (top row) and 12.3 GeV/c (bottom row) shown in bins of $\cos\theta$. Numbers in the legend refer to the center of each bin.

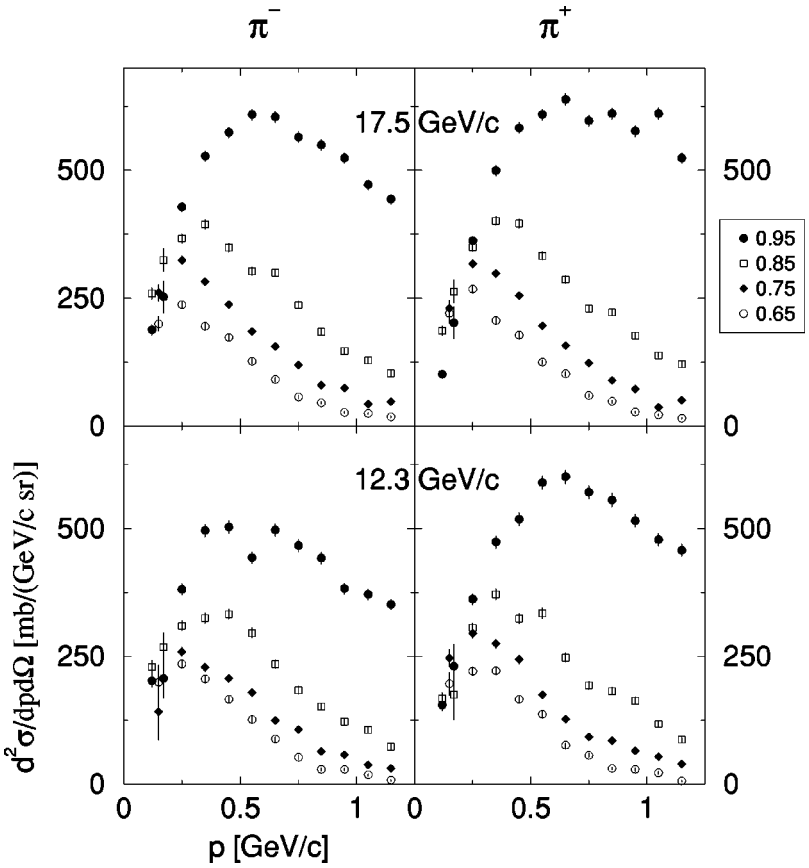

FIG. 7. Pion production cross sections for p-Cu.

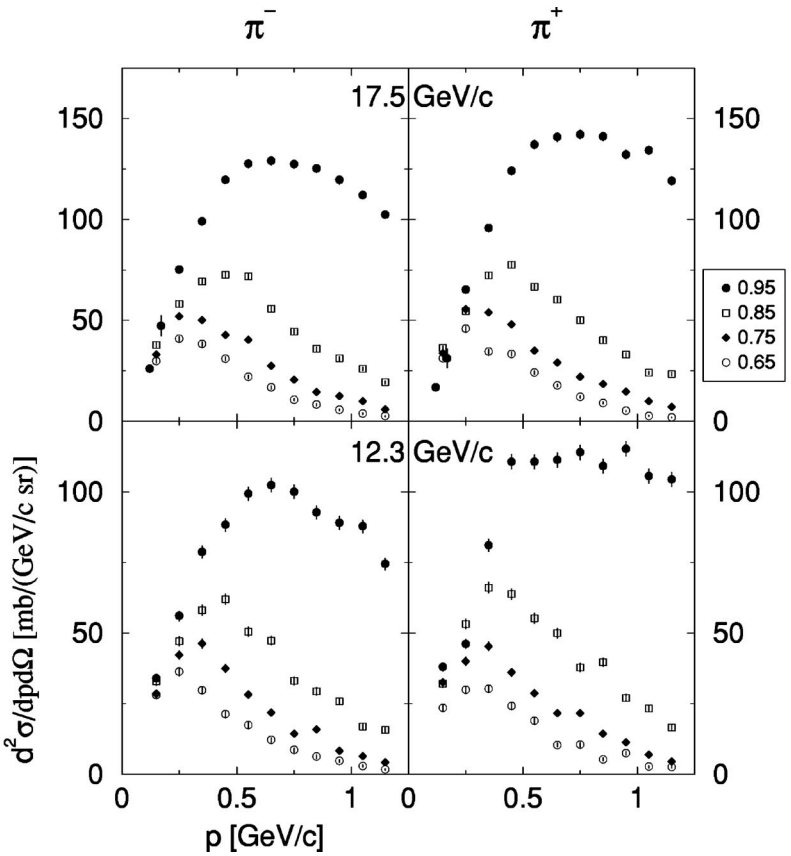

FIG. 8. Pion production cross sections for *p*-Be.

IV. RESULTS

The differential cross section for pion production for Au, Cu, and Be targets at 12.3 and 17.5 GeV/c are shown in Figs. 6–8 and Tables II–V . These were calculated in the lab frame as

$$\frac{d^2\sigma_\pi}{dp\,d\Omega}(p,\cos\theta)=\frac{A}{2\pi N_A\rho}\,\frac{1}{a(p,\cos\theta)}\,\frac{N_\pi(p,\cos\theta)}{N_b\Delta p\,\Delta\cos\theta},$$

where A is the atomic weight and N_A is Avogadro's number, N_b and ρ are the number of incoming beam particles and the area density of the target, $a(p,\cos\theta)$ stands for the acceptance, Δp and $\Delta\cos\theta$ are the bin sizes, and $N_\pi(p,\cos\theta)$ is the number of pions in the bin. We rescaled the final results by the ratio of measured interaction rates in the beam and bullseye samples. This correction ranged from 2 to 10 % and is shown in Table I. There is also a 2% uncertainty in the target thickness. We estimate the overall normalization uncertainty to be less than 5%. The errors listed are statistical, but include the uncertainty from electron background subtraction. After performing the subtraction using a Gaussian fit for the electron contamination, we chose the momentum binning such that the entire overlap region after width extrapolation was contained in a single bin. We added the uncertainty in the area of the Gaussian fit to the error bar for the signal in that bin.

We note that the spectra change from relatively flat momentum distributions in the forward direction to low-momentum peaks at higher angles. Pion production is mostly forward at higher momenta whereas it is almost isotropic at lower momenta. This is more pronounced for the heavier Au nucleus than for the lighter Be nucleus.

An interesting feature of the Au data is the large π^- excess over π^+ at the lowest momenta, which is larger at the higher beam energy. One can attribute this in part to the neutron/proton ratio of the Au nucleus. Such low-momentum pions are most likely produced through the decay of resonances and the intranuclear cascade could favor negative pions over positives. The effect is diminished for Be and Cu that have about the same number of neutrons as protons.

Looking at the 17.5-GeV/c p-Au distributions in more detail, for π^-, the peak in production shifts from about 450 MeV/c momentum in the most forward bin to about 250 MeV/c in all larger angle bins. π^+ distributions are peaked at higher momenta, around 750 MeV/c in the most forward bin and 350 MeV/c in the second forward bin, while larger angle bins look similar. π^+ and π^- yields are very close above 500 MeV/c in all except the most forward bin. The π^- excess over π^+ is most pronounced in the three most forward $\cos\theta$ bins where the π^- to π^+ ratio in the 100–140-MeV/c momentum bin is 2–3. At larger angles, the π^- and π^+ yields are close. The large π^- to π^+ yield ratio at low momenta and forward angles warrants further

TABLE II. Production cross sections for p-Au. The bin sizes are 40 and 60 MeV/c for the two lowest-momentum bins, 100 MeV/c for the rest.

		17.5 GeV/c				12.3 GeV/c			
		π^+		π^-		π^+		π^-	
cos θ	p (GeV/c)	$d^2\sigma/dp\,d\Omega$	error (stat.)	$d^2\sigma/dp\,d\Omega$	error (stat.)	$d^2\sigma/dp\,d\Omega$	error (stat.)	$d^2\sigma/dp\,d\Omega$	error (stat.)
		[mb/(GeV/c)]				[mb/(GeV/c)]			
0.95	0.12	208.3	20.5	640.4	35.9	265.8	31.5	652.2	49.3
	0.17	297.8	106.7	776.6	116.0	486.2	153.0	609.1	142.0
	0.25	817.0	25.6	1143.0	30.3	712.6	32.6	1000.1	38.6
	0.35	1146.9	30.4	1349.5	32.9	794.6	34.4	1140.5	41.3
	0.45	1305.6	32.4	1487.8	34.6	1011.7	38.9	974.1	38.1
	0.55	1304.9	32.4	1414.5	33.7	1125.7	41.0	1043.8	39.5
	0.65	1350.5	32.9	1402.3	33.6	1082.4	40.2	981.5	38.3
	0.75	1378.8	33.3	1165.3	30.6	948.0	37.6	894.9	36.5
	0.85	1277.7	32.0	1209.3	31.2	985.8	38.4	849.0	35.6
	0.95	1225.7	31.4	1045.3	29.0	906.8	36.8	749.9	33.5
	1.05	1167.6	30.6	980.9	28.1	912.6	36.9	655.1	31.3
	1.15	1004.6	28.4	1007.5	28.5	779.5	34.1	621.1	30.5
0.85	0.12	339.9	26.1	656.5	36.3	404.0	38.8	682.0	50.4
	0.17	599.1	84.5	811.4	102.6	430.9	114.2	763.2	155.7
	0.25	867.8	26.4	1091.3	29.6	824.4	35.1	815.3	34.9
	0.35	951.5	27.7	1003.6	28.4	845.7	35.5	782.7	34.2
	0.45	876.5	26.5	859.1	26.3	724.1	32.9	702.4	32.4
	0.55	758.1	24.7	759.3	24.7	743.8	33.3	685.4	32.0
	0.65	651.6	22.9	661.8	23.1	544.2	28.5	454.1	26.0
	0.75	503.0	20.1	494.7	19.9	433.4	25.4	465.0	26.3
	0.85	472.3	19.5	438.6	18.8	371.5	23.5	352.8	22.9
	0.95	404.5	18.0	390.5	17.7	302.2	21.2	327.1	22.1
	1.05	321.5	16.1	268.4	14.7	288.4	20.7	305.6	21.4
	1.15	245.1	14.0	240.4	13.9	173.5	16.1	179.3	16.4

study. There are no significant systematic effects in our tracking to bias the reconstruction against one sign. Our acceptance is also insensitive to the sign of track curvature within the region of momentum space considered in our reported results. Neutral decay contribution, on the other hand, may be appreciable and we cannot rule out the possibility that some of the asymmetry between π^+ and π^- at low momentum is due to the decays of slow Λ's. We have used the results of our 17.5-GeV/c p-Au RQMD simulation to evaluate this effect within the context of that model. Although the contribution of Λ decays to the total π^- yield below 1.2 GeV/c is small (about 3%), it is up to 8% at 100–300 MeV/c in the most forward cos θ bin and lower in the larger angle bins. The K_s decay contribution to π^+ and π^- yields in this sample is no more than 2% of the total in any bin.

ACKNOWLEDGMENTS

We thank Dr. R. W. Hackenburg and the MPS staff, J. Scaduto, and Dr. G. Bunce for their help in setting up and running the experiment. We also thank T. Schlagel and A. Stange for help with computing resources at BNL for data analysis. This work was supported by the U.S. Department of Energy under contracts with BNL (DE-AC02-98CH10886), Columbia (DE-FG02-86ER40281), ISU (DOE-FG02-92ER4069), KSU (DE-FG02-89ER40531), LBNL (DE-AC03-76F00098), LLNL (W-7405-ENG-48), ORNL (DE-AC05-96OR22464), and UT (DE-FG02-96ER40982), and the National Science Foundation under contract with Florida State University (PHY-9523974). It was also supported in part by grants from the Illinois Board of Higher Education and the Illinois Department of Commerce and Community Affairs.

TABLE III. Production cross sections for *p*-Au continued.

		17.5 GeV/c				12.3 GeV/c			
		π^+		π^-		π^+		π^-	
cos θ	p (GeV/c)	$d^2\sigma/dp\,d\Omega$	error (stat.)	$d^2\sigma/dp\,d\Omega$	error (stat.)	$d^2\sigma/dp\,d\Omega$	error (stat.)	$d^2\sigma/dp\,d\Omega$	error (stat.)
		[mb/(GeV/c)]				[mb/(GeV/c)]			
0.75	0.12	344.3	26.3	755.4	39.0				
	0.15					502.4	77.4	366.7	260.8
	0.17	392.7	101.1	828.1	119.4				
	0.25	806.2	25.5	857.3	26.2	826.4	35.1	783.6	34.2
	0.35	715.5	24.0	826.4	25.8	667.0	31.6	614.7	30.3
	0.45	629.9	22.5	648.1	22.8	562.4	29.0	571.7	29.2
	0.55	483.5	19.7	479.3	19.6	407.8	24.7	443.4	25.7
	0.65	369.9	17.2	333.4	16.4	320.4	21.9	324.9	22.0
	0.75	244.3	14.0	268.2	14.7	229.7	18.5	244.0	19.1
	0.85	204.5	12.8	207.3	12.9	153.0	15.4	217.5	18.0
	0.95	168.5	11.6	145.2	10.8	120.9	13.4	133.4	14.1
	1.05	135.6	10.4	146.6	10.9	132.2	14.0	128.0	13.8
	1.15	59.8	7.8	104.5	9.2	90.7	12.6	108.0	12.7
0.65	0.15	541.6	62.5	586.7	83.5	615.5	54.5	680.7	64.3
	0.25	676.2	23.3	671.1	23.2	643.3	31.0	616.5	30.3
	0.35	615.3	22.2	602.6	22.0	530.0	28.1	475.5	26.6
	0.45	392.1	17.8	454.0	19.1	478.0	26.7	387.4	24.0
	0.55	338.4	16.5	361.0	17.0	346.6	22.7	305.0	21.3
	0.65	251.1	14.2	273.4	14.8	193.2	17.0	207.0	17.6
	0.75	149.8	11.0	196.2	12.6	117.3	13.3	151.0	15.0
	0.85	118.8	9.8	126.3	10.1	94.9	11.9	79.7	11.4
	0.95	81.9	8.3	71.6	7.6	71.2	11.0	62.7	9.9
	1.05	55.9	6.9	59.8	6.9	99.0	12.2	56.1	9.2
	1.15	35.4	6.0	24.5	5.0	46.9	9.0	32.3	6.9
0.55	0.15	391.1	88.0	467.2	100.5				
	0.25	589.7	21.8	533.5	20.7				
	0.35	402.2	18.0	445.9	18.9				
	0.45	300.1	15.5	382.9	17.5				
	0.55	220.0	13.3	239.0	13.9				
	0.65	122.0	9.9	165.5	11.5				
	0.75	88.9	8.7	99.5	8.9				
	0.85	42.3	5.9	77.7	7.9				
	0.95	37.7	6.2	44.8	6.2				
	1.05	54.4	6.6	36.0	5.4				
	1.15	36.0	5.6	28.2	4.8				

TABLE IV. Production cross sections for *p*-Cu.

		17.5 GeV/c				12.3 GeV/c			
		π^+		π^-		π^+		π^-	
cos θ	p (GeV/c)	$d^2\sigma/dp\,d\Omega$	error (stat.)	$d^2\sigma/dp\,d\Omega$	error (stat.)	$d^2\sigma/dp\,d\Omega$	error (stat.)	$d^2\sigma/dp\,d\Omega$	error (stat.)
		[mb/(GeV/c)]				[mb/(GeV/c)]			
0.95	0.12	101.4	7.3	188.1	9.9	154.4	11.0	202.2	12.6
	0.17	201.7	31.4	252.1	31.7	229.8	43.4	206.9	38.4
	0.25	362.3	8.7	428.2	9.4	361.2	10.6	380.5	10.9
	0.35	499.2	10.2	527.5	10.5	473.4	12.2	495.6	12.5
	0.45	582.7	11.0	573.6	10.9	517.9	12.7	502.9	12.5
	0.55	608.5	11.3	608.5	11.3	589.4	13.6	442.8	11.8
	0.65	638.6	11.5	604.2	11.2	600.5	13.7	496.9	12.5
	0.75	596.4	11.1	564.5	10.8	570.3	13.4	466.5	12.1
	0.85	611.1	11.3	549.5	10.7	555.1	13.2	441.7	11.8
	0.95	576.4	11.0	524.0	10.4	514.9	12.7	382.0	10.9
	1.05	610.5	11.3	471.6	9.9	477.5	12.2	370.7	10.8
	1.15	523.7	10.4	443.5	9.6	457.3	12.0	350.9	10.5
0.85	0.12	186.2	9.8	259.1	11.6	167.4	11.4	228.7	13.4
	0.17	262.9	22.3	324.6	22.3	175.0	48.8	267.7	29.0
	0.25	349.9	8.5	366.6	8.7	305.6	9.8	309.9	9.9
	0.35	401.1	9.1	394.3	9.1	371.1	10.8	324.5	10.1
	0.45	395.9	9.1	349.3	8.5	323.8	10.1	332.6	10.2
	0.55	333.3	8.3	302.9	7.9	334.2	10.2	295.7	9.6
	0.65	286.3	7.7	299.8	7.9	247.6	8.8	234.6	8.6
	0.75	230.1	6.9	236.8	7.0	192.9	7.8	183.9	7.6
	0.85	222.6	6.8	184.3	6.2	182.1	7.6	151.8	6.9
	0.95	177.2	6.1	146.9	5.5	163.4	7.2	121.9	6.2
	1.05	138.5	5.4	128.9	5.2	117.4	6.1	105.9	5.8
	1.15	121.4	5.0	102.8	4.6	87.2	5.2	72.7	4.8
0.75	0.15	229.7	16.4	260.9	16.6	246.4	17.5	141.5	54.9
	0.25	317.0	8.1	324.3	8.2	294.2	9.6	258.6	9.0
	0.35	298.3	7.9	282.2	7.7	274.2	9.3	228.5	8.5
	0.45	254.3	7.3	237.3	7.0	243.7	8.7	206.9	8.0
	0.55	195.4	6.4	184.5	6.2	174.2	7.4	178.8	7.5
	0.65	156.5	5.7	154.6	5.7	126.8	6.3	123.8	6.2
	0.75	123.2	5.1	119.3	5.0	92.5	5.4	105.8	5.8
	0.85	89.2	4.3	79.5	4.1	84.8	5.2	63.5	4.5
	0.95	71.8	3.9	73.9	3.9	64.9	4.5	57.2	4.2
	1.05	36.0	2.7	43.0	3.0	52.9	4.1	37.3	3.4
	1.15	50.5	3.2	47.0	3.1	39.2	3.5	30.8	3.1
0.65	0.15	220.2	19.4	200.0	14.5	195.9	22.9	198.8	33.7
	0.25	267.8	7.5	237.0	7.0	220.6	8.3	234.5	8.6
	0.35	206.3	6.6	194.3	6.4	221.3	8.3	205.6	8.0
	0.45	177.5	6.1	173.0	6.0	166.0	7.2	165.7	7.2
	0.55	124.9	5.1	127.2	5.1	136.4	6.5	126.0	6.3
	0.65	102.1	4.6	90.8	4.3	76.2	4.9	87.9	5.2
	0.75	59.8	3.5	57.1	3.4	56.5	4.2	52.2	4.0
	0.85	47.8	3.2	45.3	3.1	30.6	3.1	28.7	3.0
	0.95	27.1	2.4	27.0	2.4	28.5	3.1	28.5	3.0
	1.05	21.6	2.1	24.6	2.3	22.1	2.6	18.1	2.4
	1.15	15.2	1.8	17.7	1.9	6.3	1.8	7.6	1.7

TABLE V. Production cross sections for *p*-Be.

		17.5 GeV/c				12.3 GeV/c			
		π^+		π^-		π^+		π^-	
cos θ	p (GeV/c)	$d^2\sigma/dp\,d\Omega$	error (stat.)	$d^2\sigma/dp\,d\Omega$	error (stat.)	$d^2\sigma/dp\,d\Omega$	error (stat.)	$d^2\sigma/dp\,d\Omega$	error (stat.)
		[mb/(GeV/c)]				[mb/(GeV/c)]			
0.95	0.12	16.8	1.2	26.0	1.5				
	0.15					38.1	1.5	34.0	1.4
	0.17	31.2	4.7	47.3	5.1				
	0.25	65.3	1.5	75.2	1.6	46.2	1.7	56.0	1.8
	0.35	95.8	1.8	99.1	1.9	81.2	2.2	78.7	2.2
	0.45	124.2	2.1	119.7	2.1	110.7	2.6	88.3	2.3
	0.55	137.2	2.2	127.7	2.1	110.6	2.6	99.3	2.4
	0.65	140.8	2.2	129.1	2.1	111.3	2.6	102.4	2.5
	0.75	142.2	2.2	127.5	2.1	114.0	2.6	100.0	2.4
	0.85	141.1	2.2	125.2	2.1	109.1	2.5	92.8	2.3
	0.95	132.2	2.2	119.6	2.1	115.3	2.6	89.1	2.3
	1.05	134.3	2.2	112.1	2.0	105.5	2.5	87.8	2.3
	1.15	119.1	2.1	102.4	1.9	104.4	2.5	74.4	2.1
0.85	0.15	36.3	1.1	37.9	1.2	32.2	1.4	32.9	1.4
	0.25	54.5	1.4	58.1	1.4	53.3	1.8	47.1	1.7
	0.35	72.3	1.6	69.2	1.6	66.1	2.0	58.2	1.9
	0.45	77.6	1.7	72.5	1.6	63.9	1.9	62.0	1.9
	0.55	66.6	1.5	71.8	1.6	55.3	1.8	50.5	1.7
	0.65	60.3	1.5	55.9	1.4	50.0	1.7	47.4	1.7
	0.75	50.2	1.3	44.4	1.3	37.9	1.5	33.1	1.4
	0.85	40.1	1.2	35.8	1.1	39.7	1.5	29.4	1.3
	0.95	33.1	1.1	31.2	1.0	27.1	1.3	25.9	1.2
	1.05	24.0	0.9	26.0	1.0	23.3	1.2	16.9	1.0
	1.15	23.3	0.9	19.4	0.8	16.7	1.0	15.7	1.0
0.75	0.15	33.7	1.1	33.2	1.1	32.6	1.4	28.6	1.3
	0.25	55.5	1.4	52.1	1.4	40.1	1.5	42.3	1.6
	0.35	53.9	1.4	50.0	1.3	45.4	1.6	46.3	1.7
	0.45	48.1	1.3	42.8	1.2	36.1	1.5	37.6	1.5
	0.55	35.0	1.1	40.4	1.2	28.7	1.3	28.3	1.3
	0.65	29.1	1.0	27.4	1.0	21.7	1.1	21.9	1.1
	0.75	22.1	0.9	20.6	0.9	21.7	1.1	14.5	0.9
	0.85	18.5	0.8	14.5	0.7	14.4	0.9	15.9	1.0
	0.95	14.7	0.7	12.6	0.7	11.4	0.8	8.3	0.7
	1.05	9.9	0.6	9.9	0.6	6.9	0.6	6.5	0.6
	1.15	7.1	0.5	6.0	0.5	4.6	0.5	4.3	0.5
0.65	0.15	31.3	1.1	29.8	1.0	23.6	1.2	28.1	1.3
	0.25	45.8	1.3	40.9	1.2	29.9	1.3	36.4	1.5
	0.35	34.5	1.1	38.2	1.2	30.4	1.3	29.7	1.3
	0.45	33.4	1.1	31.0	1.0	24.2	1.2	21.3	1.1
	0.55	24.2	0.9	22.0	0.9	19.0	1.1	17.5	1.0
	0.65	17.7	0.8	16.7	0.8	10.4	0.8	12.3	0.9
	0.75	12.1	0.7	10.7	0.6	10.5	0.8	8.6	0.7
	0.85	9.0	0.6	8.2	0.5	5.4	0.6	6.3	0.6
	0.95	5.1	0.4	5.8	0.5	7.4	0.7	4.8	0.5
	1.05	2.7	0.3	3.8	0.4	2.7	0.4	3.0	0.4
	1.15	1.8	0.3	2.5	0.3	2.7	0.4	1.7	0.3

[1] Y. Pang, T. Schlagel, and S. Kahana, Phys. Rev. Lett. **68**, 2743 (1992).
[2] H. Sorge, R. Mattiello, H. Stöcker, and W. Greiner, Phys. Rev. Lett. **68**, 286 (1992).
[3] C.M. Ankenbrandt *et al.*, Phys. Rev. ST Accel. Beams **2**, 081001 (1999).
[4] S. Geer, Phys. Rev. D **57**, 6989 (1998).
[5] S. Ozaki *et al.*, BNL Report No. 52623, 2001.
[6] T. Abbott *et al.*, Phys. Rev. D **45**, 3906 (1992).
[7] W.F. Baker *et al.*, Phys. Rev. Lett. **7**, 101 (1961)
[8] D. Dekkers *et al.*, Phys. Rev. **137**, B962 (1965).
[9] R.A. Lundy *et al.*, Phys. Rev. Lett. **14**, 504 (1965).
[10] G.J. Marmer *et al.*, Phys. Rev. **179**, 1294 (1969).
[11] G. Rai *et al.*, IEEE Trans. Nucl. Sci. **37**, 56 (1990).
[12] V. Karimäki, Nucl. Instrum. Methods Phys. Res. A **305**, 187 (1991).
[13] G.N. Patrick and B. Schorr, Nucl. Instrum. Methods Phys. Res. A **241**, 132 (1985).